METALURGI
Majalah Ilmu dan Teknologi
p-ISSN 0126-3188 | e-ISSN 2443-3926
ejurnalmaterialmetalurgi.lipi.go.id

STRUCTURE, MECHANICAL PROPERTIES, AND OXIDATION RESISTANCE OF Mn-RICH Fe-Mn-Al ALLOYS

Resetiana Dwi Desiati, Edi Sutiawan, Toto Sudiro, Bambang Hermanto*
Research Center for Advanced Materials, National Research and Innovation Agency
B.J. Habibie Sains and Technology Area, Banten, Indonesia 15314
*E-mail: bamb045@brin.go.id

Received: 26-07-2022, Revised: 25-10-2022, Accepted: 31-12-2022

Abstract

In this study, Mn-rich Fe-Mn-Al alloys with different Al content (Al = 0, 3, and 5 % by weight) were fabricated from ferromanganese lumps using a conventional powder metallurgy technique. The samples were compacted in 1 cm steel dies using a load of 8 tons and then sintered at 1100 ℃ for 2 h in a tubular furnace under a vacuum condition of around 0.5 mbar. To evaluate the effect of Al addition to Fe-Mn-Al alloy, the Archimedes principle and Vickers hardness were applied to estimate the density and hardness of the compact alloys. Moreover, the high-temperature oxidation resistance of the alloy was evaluated at 800 ℃ for 8 cycles. The structure of the alloy before and after oxidation was studied using XRD (x-ray diffractometer) and SEM-EDS (scanning electron microscope-energy dispersive spectrometry). The XRD analysis results show that the FeMn-0Al alloy is mainly composed Fe_3Mn_7 *phase, with the presence of FeAl phase at 3 wt.% Al, and* Al_8Mn_5 *phase at 5 wt.% Al. The density and hardness of Fe-Mn-Al alloys decreased with the increased Al content. Fe-Mn-Al alloy without Al addition exhibits poor oxidation resistance since the first cycle of the test. The results of the microstructural analysis showed that although the alloy with the addition of 3 wt.% Al showed less mass gain after being exposed for 8 cycles at 800 ℃, the Fe-Mn-Al alloy with 5 wt.% tended to be more resistant to oxidation and had no cracking defects. The structure of the oxide formed on the surface of the alloy is composed of two layers (ie; outer and inner layer) which are affected by each alloy composition.*

Keywords: *Fe-Mn-Al alloy, conventional powder metallurgy, density, hardness, oxidation*

1. INTRODUCTION

The selection of alloy composition to produce high-temperature resistant steels needs to consider the combination between mechanical properties and oxidation/corrosion resistance. Fe-Ni-Cr alloy is known to have these properties [1]-[3]. However, Ni and Cr are expensive elements, so an alternative material element is needed to replace them [2]-[4].

Previously, manganese was thought to be a key element in influencing steel microstructure, mechanical, and oxidation resistance properties [2]-[5]. It is well known that Mn is an austenite stabilizer [4], [6]. Several studies [2]-[3], [5]-[7] investigated and discussed the structure and properties of Fe-Mn steel with manganese concentrations ranging from 10% to 50% by weight . Although FeMn-based alloys have been studied [5], [8], they still have potential due to the alloy system's good properties. Because of their exceptional mechanical properties, FeMn-based alloys have been used in a variety of applications, including Hadfield steel, TWIP (twinning induced plasticity) steel [6]-[7], SMA (shape memory alloy) [9], HEA (high entropy alloy), and others [10].

The addition of alloying elements such as Al was also considered to improve the mechanical properties and the resistance of steel against oxidation at high temperatures. It is well known that Al has a high affinity for oxygen [11]-[12] and played a role in oxidation resistance, which can form a protective layer of Al-oxides and some spinels that can protect against exposure to high temperatures [11], [13]-[14]. Besides Al, Mn has also a great affinity with oxygen [8], [15], and they can react with each other to form stable oxides.

DOI : 10.14203/metalurgi.v37i3.660

Metalurgi is Sinta 2 Journal (https://sinta.ristekbrin.go.id/journals/detail?id=3708) accredited by Ministry of Research & Technology, Republic Indonesia

Over the past decades, ferromanganese lump as a source of Mn alloying elements is one of the important materials for steel production. Its name is based on the major element content in ferrolump material. This material is mostly divided into three categories: low (<0.5 wt.%), medium (<2.5 wt.%), and high (~7.0 wt.%) C content [16]. Ferro lump material has the potential to be developed because it is much cheaper than high purity metal powder which is more expensive. In this study, we used ferromanganese lumps to synthesize Mn-rich iron-manganese alloys by considering the addition of Al to determine their microstructure, mechanical properties, and oxidation resistance.

The current study focuses on the structure, hardness, and oxidation properties of Mn-rich Fe-Mn-Al alloys. Furthermore, the effect of Al content of up to 5% in weight on the aforementioned properties was thoroughly clarified and discussed.

2. MATERIALS AND METHODS

2.1 Sample Preparation

Ferromanganese lump with a chemical composition as shown in Table 1 was used in this study.

Tabel 1. Chemical composition of ferromanganese (wt.%)

Element	Wt.%
Fe	19.87
Mn	78
C	1.45
Si	0.5
P	0.15
S	0.03
Total	100

Several Fe-Mn-Al alloys with varying Al content (0, 3, and 5 wt.%) are shown in Table 2.

Tabel 2. Chemical composition of Fe-Mn-Al alloys (wt.%)

Element	FeMn-0Al	FeMn-3Al	FeMn-5Al
Fe	19.87	19.27	18.88
Mn	78	75.66	74.10
C	1.45	1.41	1.38
Si	0.5	0.485	0.475
P	0.15	0.15	0.14
S	0.03	0.029	0.029
Al	0	3	5

Al powder was used from MTIKorea with a purity of 99.9%. Firstly, the lump material (Fig. 1(a)) was crushed into powder (Fig. 1(b)) using a steel mortar and shaker mill. Subsequently, the ferromanganese powder was mixed and mechanically alloyed with different content of Al (Fig. 1(c)) as 0; 3; and 5 wt.% to obtain a uniformly mixed powder. The powder mixing was performed under wet milling condition for 2 h to avoid the powder oxidation. After that, the powder was dried in desicator.


(a) (b) (c)

Figure 1. Starting material: (a) ferromanganese lump, (b) ferromanganese powder, and (c) aluminium powder

Figure 2 shows the XRD (x-ray diffraction) spectrum of the ferromanganese and Al as the starting material. The diffraction pattern shows that ferromanganese powder is composed of Mn, $FeMn_3$, $Mn_{23}C_6$, and $Fe_{0.3}Mn_{2.7}C$ phases. While Al powder was detected by Al phase, indicating no contaminants and impurities in the powder. For the green body specimen fabrication, 2 grams of the powder was placed in steel dies with a diameter of 1 cm. The powders were uniaxially pressed using 8 tons in load for 3 min. The green body was then released from the dies and subsequently sintered at 1100 °C for 2 h in a tubular vacuum furnace under 0.5 mbar.

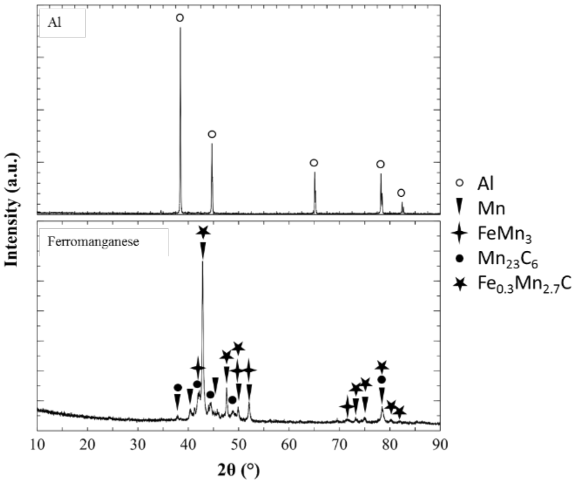

Figure 2. XRD patterns of ferromanganese and Al powder as starting material

All samples in this study were prepared using the same fabrication parameters. Following sintering, the sample's surface was mechanically polished with various grit SiC papers and DP-nap polishing for up to mirror-finish before being ultrasonically cleaned in ethanol solution. Finally, hot blowing air was used to dry the samples.

2.2 Testing and Characterization

The density and hardness of the alloys were measured using the Archimedes principle and Vickers hardness tester (LECO LM-100), respectively. The sample indentation was carried out using 300 gf for 13 s. In order to evaluate the effect of Al addition on oxidation resistance, the sample was thermally direct exposed to the atmosphere of a muffle furnace at 800 °C. The samples were soaked in the furnace at 800 °C for 20 h/cycling and rapidly cooling at ambient temperature for 4 h. This process was repeated for 8 times. The mass gain per specific area of the sample was recorded temporarily using an electronic balance KERN ABT 220-5DM (accuracy = 0.01 mg) in order to evaluate the kinetic oxidation resistance. The crystal structure, microstructure, and element distribution/chemical analysis of Fe-Mn-Al alloys before and after high-temperature oxidation test were observed by using XRD Rigaku Smartlab with CuKα1 radiation (λ=0.15405), SEM (scanning electron microscope) Hitachi SU3500 and EDS (energy dispersive spectrometry) Horiba.

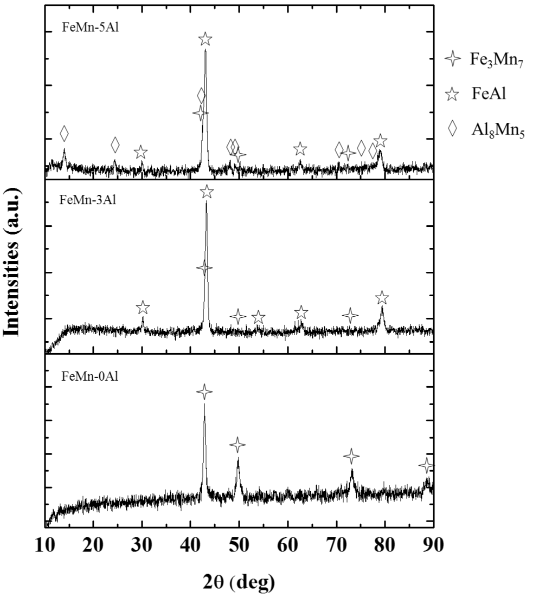

Figure 3. X-ray diffraction patterns of Fe-Mn-Al alloys with different content of Al

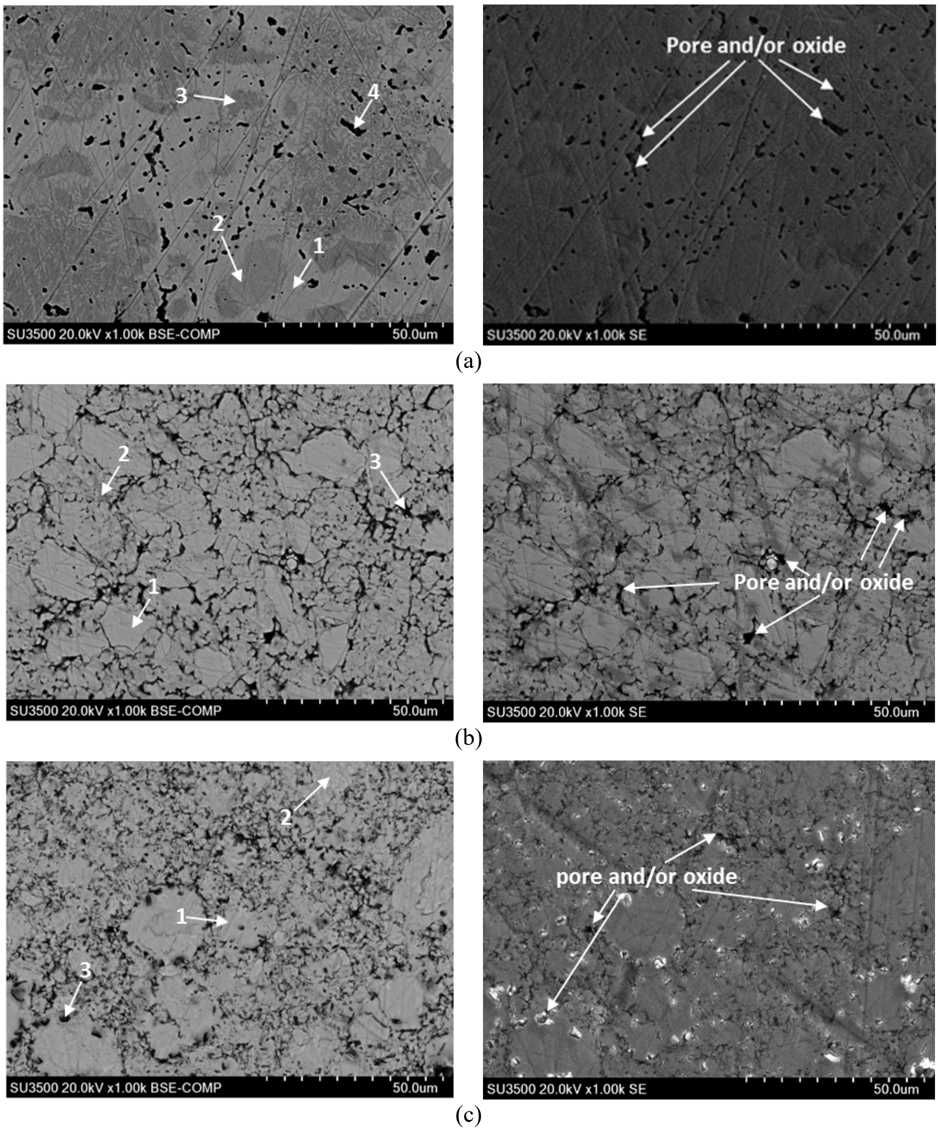

(a)

(b)

(c)

Figure 4. BSE-SE SEM surface morphologies and EDS corresponding location of Fe-Mn-Al alloys with (a) 0, (b) 3, and (c) 5 wt.% Al content

3. RESULT AND DISCUSSION

3.1 Phase Composition and Microstructure

Figure 3 shows the x-ray diffraction patterns of polished surface of Fe-Mn-Al alloys prepared by a conventional powder metallurgy technique which is vacuum sintered at 1100 °C for 2 h. As in Fig. 3, the main constituent of FeMn-0Al alloy detected by x-ray diffraction is Fe_3Mn_7 phase. Some of the diffraction peaks were not clearly visible with the addition of Al. The presence of carbides type structure is also not clearly reflected although high carbon content. It may the carbide in the same diffraction with the main detected phase, as a secondary phase of the matrix, or a mixture of phases [4]. Since carbide particles seem to be present in a small domain, the bulk technique detection by XRD may be difficult because of an overlapping peak at around 43° which makes it difficult to distinguish [17]. By addition of 3 wt.% Al, new phase was detected as FeAl. The diffraction peaks of Fe_3Mn_7 phase tends to decrease. Furthermore, with the addition of 5 wt.% of Al content, FeAl and small intensities of Fe_3Mn_7 were still detected with the appearance of a new phase of Al_8Mn_5.

Rashidi et. al., [4] reported that the manganese triggers the formation of carbides, the higher Mn will increase the concentration of carbide. In this study, an increasing the Al content will reduce the Mn content so that the carbide also tends to decrease.

The SEM (scanning electron microscope) images (BSE (backscattered electron) and SE (secondary electron)) and the corresponding location of EDS (energy dispersive spectrometry) point analysis carried out on the Fe-Mn-Al alloys sintered at 1100 °C for 2 h were shown in Fig. 4. The morphological analysis showed that the FeMn-0Al alloy had a denser and more homogeneous microstructure than the alloy with the addition of 3 and 5 wt.% of Al. Irregular black precipitates were found in Fe-Mn-Al alloys and its presence tend to increase with the addition of Al. This structure may affect the properties of alloys.

The results of BSE micrograph show that the FeMn-0Al alloy consists of three distinguished area (see Fig. 4(a)): bright (Point 1), grey (Point 2 and 3), and black areas (Point 4). Differ with Al-free alloy, the typical microstructure of 3 wt% and 5 wt% Al alloys as shown in Fig. 4(b) and 4(c) is composed of two areas mainly: grey (Point 1) and black area (Point 3). During the milling process with a shaker mill there is a collision between the ferromanganese material, steel ball, and vial. These may result an erosion from steel ball and vial that seem to be impurities. Although, due to the fact that the main element of milling balls and vial are Fe, and the ferromanganese also contains Fe. So, if there is erosion from milling balls and vials, they do not become a significant contaminant. To investigate the chemical composition of sintered Fe-Mn-Al alloys, we performed an EDS point analysis in the corresponding area of Fig. 4 and the results are listed in Table 3.

Differences in color or contrast in microstructural images from BSE SEM images usually indicate differences in elemental or phase composition of the alloy. However, point analysis (See Table 3) of EDS elements showed almost similar concentrations at all points observed in Fe-Mn-Al alloys with 0, 3, and 5 wt.% Al content. The FeMn-0Al alloy are consisting of Fe_3Mn_7 and Mn-carbide with a small concentration of Si. The concentration of Mn and C ratio was suggested as Mn_7C_3 or $Mn_{23}C_6$ phase while seen unclearly detected in the XRD result of Fig. 3.

In the FeMn-3Al alloys, the ratio of Fe, Mn, and Al content at points 1 and 2 is almost the same. It is composed of a mixture of Fe_3Mn_7, FeAl, and Mn-carbide phases. Likewise, in FeMn-5Al alloy, the Al content was detected to increase with the addition of 5 wt.% Al. The detected elements were predicted to be a mixture of Fe_3Mn_7, FeAl, Al_8Mn_5, and Mn-carbide phases.

Table 3. EDS point analysis of Fe-Mn-Al alloys: (a) FeMn-0Al, (b) FeMn-3Al, and (c) FeMn-5Al

	Point	**Element (at.%)**						**Predicted phases**
		Fe	Mn	Al	C	Si	O	
a	1	18.97	59.37	-	21.01	0.65	-	Fe_3Mn_7, Mn-carbide
	2	18.88	60.14	-	20.85	0.14	-	
	3	19.65	60.57	-	19.56	0.23	-	
	4	4.36	32.00	-	7.33	7.18	49.13	pore/oxide
b	1	9.44	40.67	21.42	28.21	0.26	-	Fe_3Mn_7, FeAl, Mn-carbide
	2	5.64	25.98	13.08	55.16	0.14	-	
	3	2.86	10.95	15.30	13.40	0.18	57.31	pore/oxide
c	1	5.76	38.02	26.33	29.76	0.14	-	Fe_3Mn_7, FeAl, Al_8Mn_5, Mn-carbide
	2	7.39	32.81	34.18	25.39	0.23	-	
	3	3.34	10.39	31.52	15.02	0.15	39.58	pore/oxide

The BSE image of Fig. 4 shows the presence of irregular black areas in all Fe-Mn-Al alloys as previously described. There are several possibilities for this area, namely pores, oxides, or a combination of these. In general, pores occur because there is not enough sintering due to several process variables as temperature and time, addition of elements, powder size, and others

[18]-[19]. High temperature can cause the evaporation of Mn during the sintering process, where it can sublimate at low temperature below the melting point [8], [15], [20]. The oxide formation may occur during the sintering process due to the high oxygen affinity of the alloying elements, which can absorb oxygen easily during powder synthesis. During milling, a significant oxidation of the particle surface can occur., oxygen can be trapped in the agglomerates, resulting in loss of ductility of the sintered sample [21]. As shown in Fig. 4, It can easily distinguish the presence of pores and oxides in sintered alloy before the oxidation test. The alloy elements are potentially oxidized during the sintering process at a vacuum pressure of about 0.5 mbar. Under these conditions, the elements that have a high affinity for oxygen to be oxidized, mostly.

The results of EDS analysis also indicate that the carbon content in all point areas is relatively high. Previous studies reported that the high carbon content may be due to the detection efficiency of light elements [22] and also on the surface of the sample, the carbon often accumulate during electron microscopy analysis [23]-[24].

It is visible from the SEM observation as shown in Fig. 4 that the Al-free alloy is denser compared to that of 3 and 5 wt.% Al alloys. Consequently, it is believed that the alloy microstructure will affect the mechanical properties of Fe-Mn-Al alloys.

3.2 Density and Hardness

The density and hardness of Fe-Mn-Al alloys with different Al content are presented in Fig. 5. The density and hardness of Fe-Mn-Al alloys decrease with the decrease of Mn and the increase of Al content.

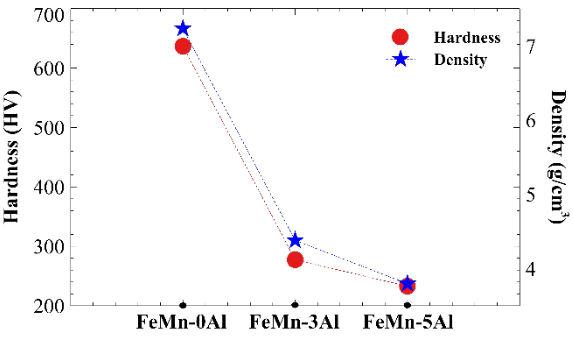

Figure 5. Density and Vickers hardness of Fe-Mn-Al alloys with different Al content

The density and hardness of FeMn-0Al alloy reached 7.127 g/cm^3 and 636.72 HV, respectively. This is reasonable when compared to pure Fe and Mn which have densities of 7.86 and 7.21 g/cm^3, respectively. On the contrary, the addition of 3 wt.% Al ($\rho \approx 2.70$ g/cm^3) leads to a decrease in density of about 4.380 g/cm^3 or almost two times lower than Al-free alloy. As Al concentration was increased to 5 wt.%, the measured density of the alloy is slightly lower than that of 3 wt% Al alloy which is 3.797 g/cm^3. Meanwhile, the hardness of the alloys decreases with the increase in Al content. It is found that the hardness of Fe-Mn-Al alloys decreases gradually to 277.37 and 232.89 HV by 3 and 5 wt.% Al addition, respectively. As with these findings, it is widely accepted that a more porous material reduces the density and hardness of the sample. This is consistent with the results of the metallographic observation described in Fig. 4. These results were correlated as reported by Rashidi et. al., [4] the hardness value is higher when manganese accumulated more in the alloys. Based on the density and properties, in general the addition of Al has been proposed to decrease the density [19], so as to further decrease the large void of the alloy [7]. In the sintering process, the addition of Al enhance material transport and increases atomic diffusion which leads to pores towards the surface of the sintered specimen [19]. This also increases the penetration of molten metal along grain boundaries. Furthermore, the addition of Al can increase sinterability and reduce the temperature of sintering process [25], which consequently increases the alloy's solubility and increases the Mn sublimation activity. The increase in Mn sublimation causes the formation of pores to increase until the end of the sintering process. At the sintering process, by adding 3 wt.% Al will possible the molten Al partially reacts with $FeMn_3$ phase to form FeAl phase. The addition of Al to 5 wt.%, except forming FeAl, molten Al also reacts with Mn and/or $FeMn_3$ to form Al_8Mn_5.

3.3 Kinetic Oxidation

The mass change of Fe-Mn-Al alloys after high temperature oxidation test at 800 °C for 8 cycles is shown in Fig. 6. Except FeMn-0Al alloys, based on the oxidation curve, it can be seen that the mass increase per unit surface area of each sample was caused by the formation of oxides during the oxidation test. It is clearly seen that Al addition significantly improved the oxidation resistance of Fe-Mn-Al alloys.

The mass gain per sample surface area of Fe-Mn-Al alloy without Al addition was dramatically decreased in the first cycle of oxidation at 800 °C, associated with a mass loss of the sample. This is due to that the sample was break suddenly after the sample was taken out from the furnace for cooling (see Fig. 7(a)).

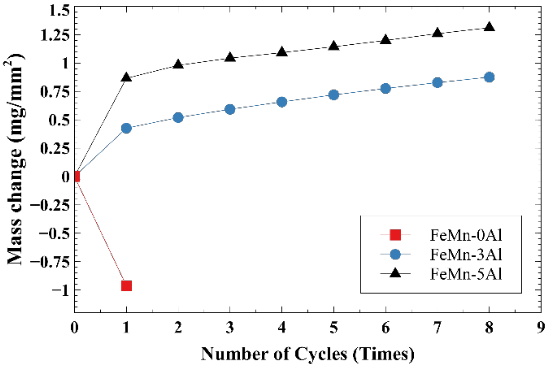

Figure 6. Oxidation curve of Fe-Mn-Al alloys after oxidation at 800 °C for 8 times

The brittle nature like a fractured surface can be observed. This deterioration and degradation could be due to the microstructure change at high temperatures [26]. It seems that there are some possible mechanisms contributing to the break of the sample during thermal shock cooling. FeMn-based alloys exhibit a shape memory effect undergoing fcc - hcp phase transformation, and there is a defect accumulation during temperature change [9]. The oxidation cycle may affect the phase strain at the heat-cooling cycle and phase reorientation. This happens and causes the accumulation of defects during the continued oxidation cycle. The mechanical properties of Fe-Mn steels are affected and depend on Mn content as reported by Kim et. al., [3] while as the Mn content increases, the ductile to brittle as the temperature changes.

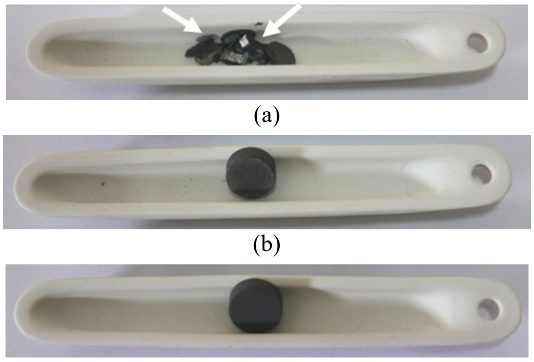
(a)

(b)

(c)

Fig. 7. Photograph of Fe-Mn-Al alloys with (a) 0, (b) 3, and (c) 5 Al after oxidation at 800 °C for 1 cycle

Some parts of the sample were break to the outside of alumina crucible, resulting in mass gain decreasing. For this reason, the high-temperature oxidation test of FeMn-0Al alloy was stopped in the first cycle. Interestingly, the aforesaid evidence doesn't occur in the Al-added alloy. It can be seen that the mass gain of the sample increase with the increase of Al concentration in the alloys (Fig. 6). The mass gain of 5 wt.% Al alloys is two time higher compared to that of 3 wt.% Al alloy.

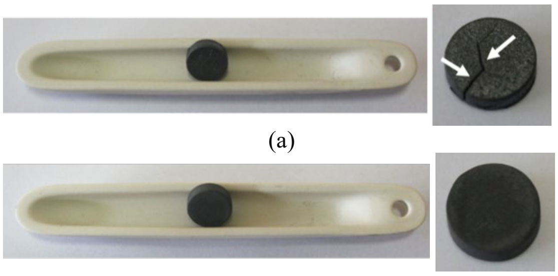
(a)

(b)

Figure 8. Photograph of Fe-Mn-Al alloys with (a) 3 and (b) 5 Al after oxidation at 800 °C for 8 cycles

Based on the results as presented above (see Fig. 8), it should be pointed out that although 3 wt.% Al alloy exhibit the lowest mass gain after exposure for 8 cycles at 800 °C, the alloy is susceptible to the oxidation induce crack formation.

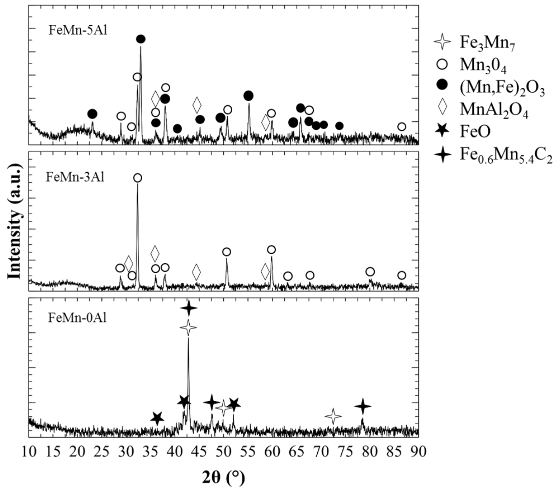

Figure 9. X-ray diffraction patterns of Fe-Mn-Al alloys with different content of Al after exposure at 800 °C for FeMn-0Al in 1 cycle, and FeMn-3Al and FeMn-5Al in 8 cycles

3.4 Phase Composition and Microstructure after Oxidation Test at 800 °C

The x-ray diffraction patterns of Fe-Mn-Al alloys after a high-temperature oxidation test at 800 °C was shown in Fig. 9. There are some different compositions of oxide scale formed on Fe-Mn-Al alloys after the oxidation test at 800 °C. The FeMn-0Al alloy forms mainly FeO scales. Since FeMn-0Al alloy gets a breakaway in the first cycle, the Fe_3Mn_7 phase was still detected, and carbide is $Fe_{0.6}Mn_{5.4}C_2$ like as XRD detected. The FeMn-3Al consists Mn_3O_4 and $MnAl_2O_4$ scales. Meanwhile, FeMn-5Al contains of Mn_3O_4, $MnAl_2O_4$, and $(Mn, Fe)_2O_3$ scales. Besides that, it looks like an increase of background in the 2θ range of 15 to 30 degrees which may the oxidized alloys have an amorphous phase.

Figure 10 shows the cross-sectional SEM images and EDS point analysis of Fe-Mn-Al alloys after the oxidation test at 800 °C for 8 cycles. While Figure 11 presents its EDS mapping analysis. Based on the contrast and brightness, the oxide layer can be divided into two main layers, namely the inner layer and the outer layer. Fe, Mn, Al, C, Si, and O elements are seen scattered in the oxide layer. The thickness of the oxide layer after exposure at 800 °C for 8 cycles, was from 50 to 60 μm and 40 to 50 μm on the FeMn-3Al and FeMn-5Al alloys, respectively.

Attention was directed to a contrast difference between the interface of the inner layer to the inside of the alloy as shown in Figure 10 (See yellow-dash arrow). This can be correlated with the BSE morphology of the cross-sectional Fe-Mn-Al alloys, especially for the Mn elements. This likely occurs an Mn depletion of the Fe-Mn-Al alloys. The Mn content increased from the inner layer towards the FeMn-3Al and 5Al alloys. It is as reported by Xu et. al., [20] Mn content increases parabolically, starting from the resin-sample interface of the sintered samples.

Based on Fig. 10, the microstructure had a random distribution from the interface scale to the inside of the alloys. Although they can be distinguished, by contrast, there are some areas that look the same but still contain other elements. The results of EDS point analysis were performed to examine the elemental composition of scales and the sintered alloys after oxidation as listed in Table 4. Furthermore, the predicted phases on those points were then confirmed by XRD and EDS mapping analysis.

Pont 1 on FeMn-3Al are composed mainly of Si, Al, Mn, Fe, and O. Thus, almost the same to point 1, point 2 mainly consists of Si, Fe, Mn, Al, and O. Point 1 and point 2 predicted to as SiO_2, and the mixture of (Fe, Mn, Al)-oxide. Point 3 and point 4 are composed of Mn, Fe, and O, and a small amount of Al and Si are predicted as Mn_3O_4 and $MnFe_2O_4$. The Si content in points 1 and 2 is higher than in points 3 and 4, while the Mn content is more at points 3 and 4. Based on the results, outer-layer is mainly consisted of the SiO_2 phase and the inner layer is Mn_3O_4. Meanwhile, a mixture of oxides (Fe, Mn, Al) as $MnAl_2O_4$ and Mn_3O_4 is spread on outer layer.

In FeMn-5Al alloy, point 1 in the outer layer is composed of Si, Al, Mn, Fe, and O which are predicted as SiO_2 and the mixed oxide of (Fe, Mn, Al). Elsewhere in the outer layer, point 2 contains Mn, Al, Si, Fe, and O. Although it contains mainly Mn, this area is still influenced by Si content as in point 1. Point 2 is predicted as Mn_3O_4, $MnAl_2O_4$, SiO_2, and a little amount of $MnFe_2O_4$. Point 3 containing a high concentration of Mn and O is predicted as Mn_3O_4. Whereas Point 4 is mainly composed of Mn, Al, O, and a small concentration of Fe that is predicted as Mn_3O_4 and Al_2O_3.

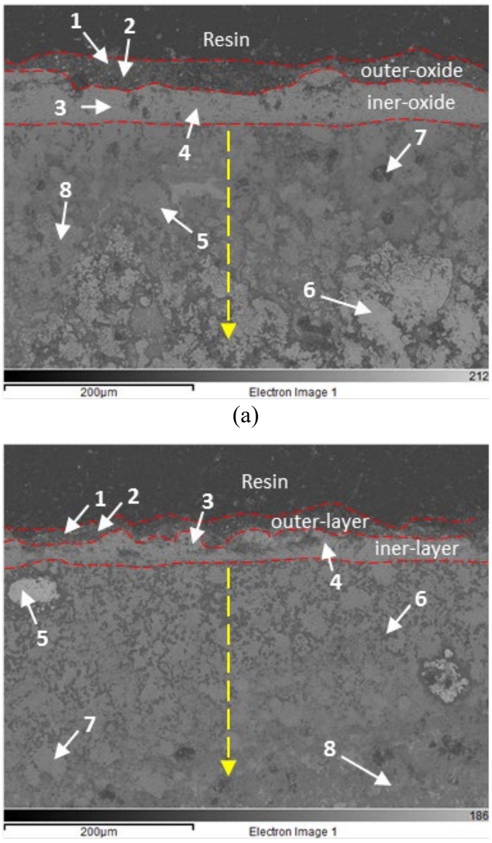

(b)

Figure 10. The cross-sectional SEM images and the corresponding EDS point analysis of (a) 3 and (b) 5 wt.% Al alloys after oxidation test at 800 °C for 8 cycles

Beneath the oxide layer there are oxygen concentrations at points (5, 6, 7, and 8), and (5, 6, and 7) in FeMn-3Al and FeMn-5Al alloys, respectively. This evidence indicates that there is internal oxidation occurs inside alloys. Firstly, during the initial oxidation due to the presence of pores oxygen freely diffuses into the alloy and reacts with the elements. The pores can become access or diffusion paths between the elements and reacting oxygen when the oxidation test is carried out at a temperature of 800 °C. This access is formed from an area called the depleted zone Mn as described previously.

The results of the EDS mapping analysis indicate the concentrations of Al and O have high contrast. These may react with each other to form Al-oxide, along with other elements. It is possible because Al has a high affinity to oxygen [12]. It is also confirmed from the EDS mapping of Fig. 11 that there are concentrations rich in Mn, Al, and O in FeMn-3Al and rich in Fe, Mn, Al, and O in FeMn-5Al under the inner oxide.

The addition of Al to Fe-Mn-Al alloys may encourage the formation of Al-oxides and/or their mixtures which then could become more of a barrier or barrier for the next diffusion process, so this causes the thickness of FeMn-5Al scales to be thinner than FeMn-3Al alloy. The previous studies report that an Al_2O_3 has a low oxygen diffusion rate, which can act as a barrier to oxygen diffusion [6], [13]. Although Al-oxide is not detected by XRD because it is not possible to measure deeper into the alloy, this is the reason why it does not form on the alloy surface even though the oxide is more protective when formed at the alloy surface or interface.

Table 4. EDS point analysis of Fe-Mn-Al alloys after oxidation test at 800 °C: (a) 0Al, (b) 3Al, and (c) 5Al

Point		Element (at%)					Predicted phases
		Fe	Mn	Al	Si	O	
a	1	1.98	3.54	5.71	53.59	35.19	SiO_2,
	2	5.75	5.13	4.12	50.03	34.96	(Fe,Mn,Al) oxide
	3	8.31	31.24	0.79	0.05	59.62	Mn_3O_4,
	4	7.32	29.84	0.83	0.06	61.94	$MnFe_2O_4$
	5	10.02	20.88	10.79	0.16	58.15	(Fe,Mn,Al) oxide
	6	22.38	54.23	15.63	0.91	6.85	Fe_3Mn_7, Al_2O_3
	7	11.65	17.65	31.34	3.42	35.94	Fe_3Mn_7, Al_2O_3
	8	4.44	11.05	23.44	0.09	60.98	Fe_3Mn_7, Al_2O_3
b	1	8.59	11.24	15.15	23.03	41.99	SiO_2, (Fe,Mn,Al) oxide
	2	2.83	39.09	10.51	7.96	39.61	Mn_3O_4, $MnAl_2O_4$, SiO_2 $MnFe_2O_4$
	3	1.21	34.93	0.58	0.22	63.05	Mn_3O_4
	4	2.74	37.87	6.99	0.60	51.79	Mn_3O_4, Al_2O_3
	5	52.72	45.99	0.30	0.41	0.58	Fe_3Mn_7
	6	1.83	2.88	33.56	0.13	61.11	Al_2O_3
	7	7.66	20.12	11.78	0.20	60.25	Fe_3Mn_7, Al_2O_3
	8	2.86	11.72	24.10	0.14	61.18	Fe_3Mn_7, Al_2O_3

The difference contrast was also seen between Fe, Mn, and O concentrations in FeMn-3Al and FeMn-5Al which correspond to inner oxide layer. The presence of Fe, Mn, and O in the inner layer, suggests it is composed of $MnFe_2O_4$ scales. Besides that, the distribution of Mn, Al, and O in the outer layer can also be observed. As seen in Fig. 11, the Al distribution in FeMn-5Al is more clear than in the FeMn-3Al alloy. It can be correlated to the presence of the $MnAl_2O_4$ scale as detected by XRD. This is also confirmed as a mixture of (Fe, Mn, and Al)-oxide predicted on EDS point analysis. Kurokawa et. al., [14] report the addition of Al in Fe-Cr-Mn alloys increases oxidation resistance by the formation of spinel oxide $MnAl_2O_4$ which contributes to the suppression of pore formation.

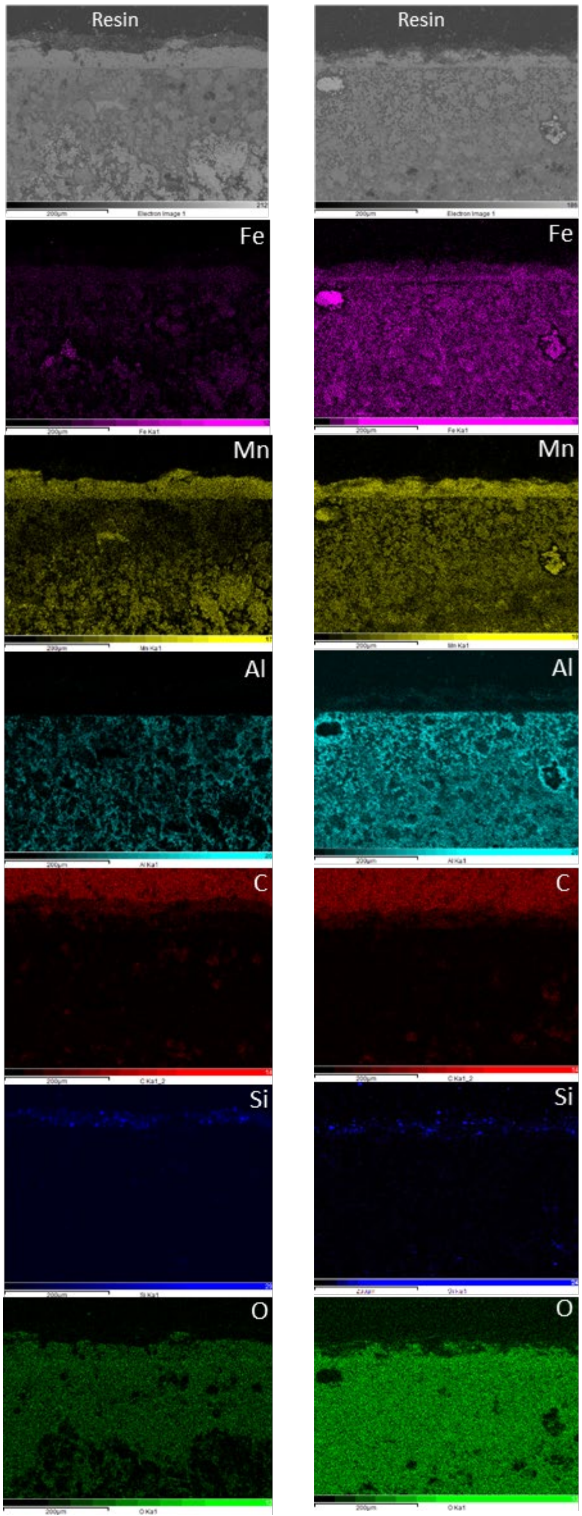

(a) (b)

Figure 11. BSE cross-sectional morphologies and EDS mapping of Fe-Mn-Al alloys with (a) 3 and (b) 5 wt.% Al content after oxidation at 800 °C for 8 cycles

The distribution of Si content in the outer layer can also be seen in Fig. 11. Si may have combined with Fe and Mn elements to form an oxide mixture. However, elemental point analysis reveals Si content, whereas XRD analysis does not. It is feasible in the form of amorphous SiO_2, which appears as background noise in the XRD spectrum.

On the other hand, even though the O content is widely distributed, the distribution of C concentration tends to slightly decrease on the inside of the sintered sample after oxidation. Evaporation appears to occur when oxidation from the carbide phase reacts with oxygen to form CO and/or CO_2 gaseous, leaving the initial location and forming pores. It causes the formation of microcracks, resulting in a faster diffusion path [6]. Furthermore, the carbon oxidation decreases after the formation of the $MnAl_2O_4$, $MnFe_2O_4$, and Al_2O_3 scales, as do the oxidation times.

Based on the results of this study, it was found that the oxide layer formed on the FeMn-3Al alloy has the best oxidation resistance but breakaway oxidation occurs. The increase of 5 wt% Al content evident could prevent crack defects during high-temperature exposures at 800 °C due to the presence of Al-oxide or their oxide mixtures. The higher Al content provides more possibility of Al- oxide formation which can heal porous defects and enhance the prevention of carbon oxidation during high-temperature exposures. This is also the reason why the addition of Al has a significant contribution to the growth of scales.

4. CONCLUSION

In this study, the effect of Al addition on the structure, density, hardness, and high-temperature oxidation resistance of Fe-Mn-Al alloys has been presented and discussed. Based on the results obtained, the microstructure homogeneity of the Fe-Mn-Al alloy decrease with the increase of Al content. Irregular black area precipitates were found in Fe-Mn-Al alloys and their presence tends to increase with the addition of Al. The density and hardness of Fe-Mn-Al alloys decrease with the decrease of Mn and the increase of Al content. The Al addition leads to a significantly improved oxidation resistance of Fe-Mn-Al alloys. The Fe-Mn-Al alloy by 5 wt.% Al exhibits good resistance toward oxidation at 800 °C for 8 cyclic and had no cracking defects. Although shows a better oxidation curve than FeMn-5Al, the presence of cracks is found in FeMn-3Al alloy. During oxidation, the presence of the Al8Mn5 phase in the FeMn-5Al alloy causes the formation of Al-oxide and/or their mixture, which acts as a barrier and heals aporous defects.

ACKNOWLEDGMENT

The authors would like to thank the Research Center for Advanced Materials, National Research and Innovation Agency (BRIN) for providing processing and characterization facilities.

REFERENCES

[1] X. W. Zhou, M. E. Foster, and R. B. Sills, “An Fe-Ni-Cr embedded atom method potential for austenitic and ferritic systems,” *J. Comput. Chem.*, vol. 39, no. 29, pp. 2420-2431, 2018. Doi: 10.1002/jcc.25573.

[2] M. B. Abuzriba and S. M. Musa, “Substitution for chromium and nickel in austenitic stainless steels,” in *2nd International Multidisciplinary Microscopy and Microanalysis Congress*, vol. 164, E. K. Polychroniadis, A. Y. Oral, and M. Ozer, Eds. Cham: Springer International Publishing, 2015, pp. 205-214. Doi: 10.1007/978-3-319-16919-4_27.

[3] J.-S. Kim, S. Yong Shin, J. Eun Jung, J. Young Park, and Y. Won Chang, “Effects of tempering temperature on microstructure and tensile properties of Fe-12Mn steel,” *Mater. Sci. Eng. A*, vol. 640, pp. 171-179, 2015. Doi: 10.1016/j.msea.2015.05.036.

[4] M. Mohd. Rashidi and Mohd. Hasbullah Idris, “Microstructure and mechanical properties of modified ductile Ni-resist with higher manganese content,” *Mater. Sci. Eng. A*, vol. 574, pp. 226-234, 2013. Doi: 10.1016/j.msea.2013.02.038.

[5] A. Mondal, D. Pilone, A. Brotzu, and F. Felli, “Effect of heat treatment on mechanical properties of FeMnAlC alloys,” *Procedia Struct. Integr.*, vol. 33, pp. 237-244, 2021. Doi: 10.1016/j.prostr.2021.10.029.

[6] W. Peng, Z. Wu, Y. Xu, Q. Ran, W. Xu, J. Li, and X. Xiao, “Internal oxidation behaviour of Fe-Mn-Al-C duplex light-weight steels with good combination of strength and ductility,” *Corros. Sci.*, vol. 120, pp. 148-157, 2017. Doi: 10.1016/j.corsci.2017.03.005.

[7] J.-E. Jin and Y.-K. Lee, “Effects of Al on microstructure and tensile properties of C-bearing high Mn TWIP steel,” *Acta Mater.*, vol. 60, no. 4, pp. 1680-1688, 2012. Doi: 10.1016/j.actamat.2011.12.004.

[8] A. Šalak, M. Selecká, and R. Bureš, “Manganese in ferrous powder metallurgy,” *Powder Metall. Prog.*, no. 1,

pp. 19, 2001.

[9] M. E. Evard, A. A. Volkov, F. S. Belyaev, A. D. Ignatova, and N. A. Volkova, "Microstructural modelling of plastic deformation and defects accumulation in FeMn-based shape memory alloys," *Procedia Struct. Integr.*, vol. 2, pp. 1546-1552, 2016. Doi: 10.1016/j.prostr.2016.06.196.

[10] P. Chowdhury, D. Canadinc, and H. Sehitoglu, "On deformation behavior of Fe-Mn based structural alloys," *Mater. Sci. Eng. R Rep.*, vol. 122, pp. 1-28, 2017. Doi: 10.1016/j.mser.2017.09.002.

[11] L. Stratil, V. Horník, P. Dymáček, P. Roupcová, and J. Svoboda, "The influence of aluminum content on oxidation resistance of new-generation ODS alloy at 1200 °C," *Metals*, vol. 10, no. 11, pp. 1478, 2020. Doi: 10.3390/met10111478.

[12] J. Gao, Shixi Liu, Xiaojun Wang, and Wenbin Wang, "Effects of high oxygen-affinity elements on microstructure of Cu-Cr alloy ingots," in *2013 2nd International Conference on Electric Power Equipment - Switching Technology (ICEPE-ST)*, Matsue-city, Japan, pp. 1-4, 2013. Doi: 10.1109/ICEPE-ST.2013.6804309.

[13] X. Zhang, Z. Deng, H. Li, J. Mao, C. Deng, C. Deng, S. Niu, W. Chen, J. Song, J. Fan, M. Liu, and K. Zhou, "Al_2O_3-modified PS-PVD 7YSZ thermal barrier coatings for advanced gas-turbine engines," *Npj Mater. Degrad.*, vol. 4, no. 1, pp. 31, 2020. Doi: 10.1038/s41529-020-00134-5.

[14] K. Kurokawa, Y. Mizuta, and H. Takahashi, "Oxidation of Fe-Cr-Mn-Al stainless steels," in *High Temperature Corrosion of Advanced Materials and Protective Coatings*, Elsevier, pp. 91-96, 1992. Doi: 10.1016/B978-0-444-88970-6.50015-4.

[15] A. Šalak and M. Selecká, "Thermodynamic conditions for the Mn–O system in sintering of manganese steels," in *Manganese in Powder Metallurgy Steels*, Cambridge: Cambridge International Science Publishing Ltd., pp. 5-21, 2012. Doi: 10.1007/978-1-907343-75-9_2.

[16] B.-D. You, B.-W. Lee, and J.-J. Pak, "Manganese loss during the oxygen refining of high-carbon ferromanganese melts," *Met. Mater.*, vol. 5, no. 5, pp. 497-502, 1999. Doi: 10.1007/BF03026165.

[17] S. T. Oyama, Ed., *The Chemistry of Transition Metal Carbides and Nitrides*. Dordrecht: Springer Netherlands, pp. 530, 1996. Doi: 10.1007/978-94-009-1565-7.

[18] N. Kurgan, "Effect of porosity and density on the mechanical and microstructural properties of sintered 316L stainless steel implant materials," *Mater. Des.*, vol. 55, pp. 235-241, 2014. Doi: 10.1016/j.matdes.2013.09.058.

[19] H. Sazegaran, H. Bahari, A. M. Naserian-Nik, and F. Khorramshahi, "Archives of metallurgy and materials archives of metallurgy and materials," vol. 67, no. 1, pp. 105-111, 2022. Doi: 10.24425/AMM.2022.137478.

[20] Z. Xu, M. Hodgson, K. Chang, G. Chen, X. Yuan, and P. Cao, "Effect of sintering time on the densification, microstructure, weight loss and tensile properties of a powder metallurgical Fe-Mn-Si Alloy," *Metals*, vol. 7, no. 3, pp. 81, 2017. Doi: 10.3390/met7030081.

[21] A. Bolsonella, F. Naimi, O. Heintz, T. Tricone, H. Couque, and F. Bernard, "Influence of oxygen induced during high-energy ball milling process on the mechanical properties of sintered nickel by SPS," *J. Alloys Compd.*, vol. 856, pp. 157869, 2021. Doi: 10.1016/j.jallcom.2020.157869.

[22] F. C. Miguens, M. L. d. Oliveira, R. V. Marins, and L. D. d. Lacerda, "A new protocol to detect light elements in estuarine sediments by X-ray microanalysis (SEM/EDS)," *J. Electron Microsc. (Tokyo)*, vol. 59, no. 5, pp. 437-446, 2010. Doi: 10.1093/jmicro/dfq013.

[23] J. Konopka and T. F. Scientific, "Options for quantitative analysis of light elements by SEM/EDS," Technical Note, pp. 1-2, 2013.

[24] L. L. A. Nisa, B. Hermanto, S. Aritonang, M. T. E. Manawan, and T. Sudiro, "Mechanical properties and high-temperature oxidation of (WC-12Co) + $MoSi_2$ hardmetals," *Int. J. Refract. Met. Hard Mater.*, vol. 109, pp. 10, 2022. Doi : 10.1016/j.ijrmhm.2022.105987

[25] H. Ghezelbash, A. Zeinali, N. Ehsani, and H. R. Baharvandi, "The effect of aluminum additive on pressureless sintering of SiC," *J. Aust. Ceram. Soc.*, vol. 55, no. 4, pp. 903-911, 2019. Doi: 10.1007/s41779-019-00310-0.

[26] A. M. Babakr, A. Al-Ahmari, K. Al-

Jumayiah, and F. Habiby, “Sigma phase formation and embrittlement of cast iron-chromium-nickel (Fe-Cr-Ni) alloys,” *J. Miner. Mater. Charact. Eng.*, vol. 07, no. 02, pp. 127-145, 2008. Doi: 10.4236/jmmce.2008.72011.